Respiratory Physiology & Neurobiology 325 (2024) 104265

Contents lists available at ScienceDirect

Respiratory Physiology & Neurobiology

journal homepage: www.elsevier.com/locate/resphysiol

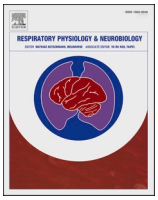

Airway stability in sleep apnea: Assessing continuous positive airway pressure efficiency

Suvash C. Saha [1,*], Xinlei Huang [1], Isabella Francis, Goutam Saha

School of Mechanical and Mechatronic Engineering, Faculty of Engineering and Information Technology, University of Technology Sydney, Sydney, NSW, Australia

ARTICLE INFO

Edited by Mathias Dutschmann

Keywords:
Continuous positive air pressure
Respiratory tract, Obstructive sleep apnea
Computational fluid dynamics

ABSTRACT

Obstructive Sleep Apnea Syndrome (OSAS) disrupts millions of lives with its burden of airway obstruction during sleep. Continuous Positive Airway Pressure (CPAP) therapy has been scrutinized for its biomechanical impact on the respiratory tract. This study leverages computational fluid dynamics to investigate CPAP's effects at 9 cm H_2O (882.6 Pa) on the computed-tomography-based nasal-to-14-generation full respiratory tract model compared to ambient conditions, focusing on static pressure, airflow velocity, and shear stress. Our findings reveal that CPAP significantly increases static pressure, enhancing airway patency without adverse changes in airflow velocity or harmful shear stress on lung tissue, challenging prior concerns about its safety. Notably, the larynx experiences the highest shear stress due to its narrow anatomy, yet CPAP therapy overall supports airway walls against collapse. This investigation highlights CPAP's critical role in OSAS treatment, offering reassurance about its safety and efficacy. By clarifying CPAP therapy's physiological impacts, our study contributes vital insights for optimizing OSAS management strategies, affirming CPAP's benefit in maintaining open airways with minimal tissue strain.

1. Introduction

Obstructive sleep apnea syndrome (OSAS) is a chronic condition that arises during sleep when the throat muscles temporarily relax, leading to narrowed or obstructed airway passage. These episodes can occur repeatedly throughout the night, lasting from a few seconds to several minutes. It is estimated that approximately 2–4 % of adults in the United States and about 4.63 % of adults in China experience this condition, which significantly affects their daily lives. OSAS can result in excessive daytime sleepiness and a higher risk of health issues such as high blood pressure, heart disease, diabetes, and other related complications (Zhu et al., 2019a).

In the last two decades, the use of computational fluid dynamics (CFD) has significantly increased (Huang et al., 2022), profoundly transforming our understanding of physiological processes in both health and disease states (Saha et al., 2024). Xu et al.'s (2006) study on airway pressure and flow using a physical upper airway model highlights the pharynx and nasal cavity's role in airway collapse. Strohl et al. (2012). focused on the upper airway's mechanical properties, noting the importance of biomechanical analysis in understanding sleep apnea and related conditions. Jeong et al. (2007) identified velopharynx sensitivity in OSAS development, emphasizing the need for targeted management strategies. Yu et al. (2012) demonstrated CFD simulations' potential in revealing OSAS mechanisms and the impact of anatomical structures on its development, suggesting CFD's value in OSAS research. Huang et al. (2013) explored OSAS control mechanisms using FSI and CFD, revealing insights into flow dynamics and the benefits of FSI for understanding pressure increases in narrowed airways. Lu et al. (2014). demonstrated surgical treatment's effectiveness in reducing flow resistance and wall shear stress in severe OSAS patients through Large Eddy Simulation. Luo et al. (2014). found surgical interventions notably improved conditions in overweight children with OSAS, reducing symptoms and airway pressure. Wootton et al. (2014). identified that children with OSAS and higher body weights have narrower airways and increased pressure, compared to healthy controls, using CFD and statistical analyses. Cisonni et al. (2015). investigated inhalation flow patterns, suggesting detailed modeling of the nasal cavity may not be crucial for accurate pharyngeal pressure predictions. Taherian et al. (2019a). linked OSAS severity to flow velocity, pressure drop, and wall shear stress in the velopharynx, emphasizing the role of these factors in OSAS. Faizal et al. (Rahim et al., 2021). observed that turbulent kinetic energy could

* Corresponding author.
E-mail address: Suvash.Saha@uts.edu.au (S.C. Saha).
[1] S.C. Saha and X., Huang contributed equally

https://doi.org/10.1016/j.resp.2024.104265
Received 14 March 2024; Received in revised form 11 April 2024; Accepted 19 April 2024
Available online 21 April 2024

Nomenclature

Roman symbols

g	Gravitational acceleration, in the negative z-direction (ms^{-2})
k	Turbulence kinetic energy(m^2s^{-2})
p	Static pressure (Pa)
t	Time (s)
$\boldsymbol{u}$	Fluid velocity vector (ms^{-1})
G_b	Turbulence generation due to buoyancy
$G_{\omega b}$	Turbulence generation due to buoyancy for ω equation
P_k	Rate of production of turbulent kinetic energy
P_ω	Rate of production of specific dissipation rate
S_{ij}	Mean component of the rate of deformation s_{ij}
Y_k	Dissipation of turbulent kinetic energy due to turbulence
Y_ω	Dissipation of specific dissipation rate due to turbulence

Greek symbols

σ_k	Turbulent Prandtl numbers for turbulent kinetic energy
σ_ω	Turbulent Prandtl numbers for the specific dissipation rate
μ	Molecular viscosity of the fluid (Nsm^{-2})
μ_t	Turbulent viscosity (Nsm^{-2})
ν	Kinematic viscosity of the fluid (m^2s^{-1})
ρ	Fluid density (kgm^{-3})
$\bar{\bar{\tau}}$	Stress tensor (Pa)
ω	Specific dissipation rate (s^{-1})

significantly assess OSAS severity, highlighting its importance in understanding upper airway flow characteristics in OSAS patients.

The current literature on treating OSAS with CPAP suggests it as the most effective method compared to alternatives like Mandibular advancement devices, positional therapy, and hypoglossal nerve stimulation (Gambino et al., 2022). Zhao et al. (2013). developed an FSI model to study the effects of Mandibular Advancement Splint treatment on OSAS, indicating it could enhance understanding of upper airway dynamics. Suga et al. (2021). highlighted the importance of CFD in assessing airway pressure and velocity with oral appliances for OSAS treatment. Zhu et al. (2019b). used CFD to examine the efficacy of H-uvulopalatopharyngoplasty in OSAS, showing airway expansion and reduced negative pressure. Wakayama et al. (2016). found that CPAP at 10 cm H_2O improves airflow in narrowed nasal passages, enhancing respiratory function. Abdullayev et al. (2019). demonstrated that OSAS patients have a higher risk of Glaucoma, which CPAP treatment can mitigate. Reynor et al. (2022). cautioned the varying effectiveness of CPAP in preventing cardiovascular incidents in OSAS patients, suggesting the need for individualized treatment considerations.

The existing body of literature highlights a notable research gap in the context of OSAS across diverse patient populations. The predominant focus of previous CFD numerical studies of CPAP therapy has been directed toward examining flow dynamics and pressure variations exclusively within the nasal cavity, overlooking the potential contribution of other pertinent factors to CPAP therapy. Previous studies, such as those conducted by Xu et al. (2006), Jeong et al. (2007), and Lu et al. (2014), have employed various computational approaches to investigate the relationship between anatomical features and their contributions to OSAS pathophysiology. However, these studies do not account for the dynamic changes introduced by CPAP therapy, particularly in terms of static pressure, airflow velocity, and shear stress across the entire respiratory tract. Moreover, while studies like those by Yu et al. (2012) and Huang et al. (2013) have begun to explore the potential of CFD simulations to understand OSAS mechanisms, there remains a substantial need for a comprehensive examination that captures the detailed effects of CPAP on airway dynamics.

Therefore, our study seeks to bridge this gap by utilizing state-of-the-art CFD analysis to conduct a comprehensive examination of the respiratory tract under CPAP therapy. Our innovative approach not only assesses the static pressure, airflow velocity, and shear stress within a complete respiratory tract model but also evaluates CPAP's overall impact on respiratory system dynamics. By offering both qualitative and quantitative analyses, our research provides new insights into the physiological changes induced by CPAP therapy, advancing our understanding of its effectiveness and safety in treating OSAS. This study's novelty lies in its holistic examination of the CPAP's impact, moving beyond the confines of the nasal cavity to explore the effects of CPAP across the entire respiratory tract. Our findings aim to contribute significantly to the body of knowledge on CPAP therapy, offering a more detailed understanding of its therapeutic potential and guiding future research and clinical practice in managing OSAS.

2. Methodology

2.1. Anatomical features of the respiratory tract

This study develops a comprehensive computational model of the human respiratory tract, with the methodology detailed available in our previous work (Saha et al., 2022; Huang et al., 2024). The respiratory tract was divided into specific lobes and regions to improve mesh creation and post- simulations data analysis, as depicted in Figs. 1a and 1b. Geometric details and specifications are provided in Appendix A.

2.2. Fluid dynamics

This study employs continuity and momentum equations to model the dynamics governing the respiratory tract's aerodynamics. Furthermore, the k–ω Shear Stress Transport (SST) turbulence model is employed to capture the turbulence phenomenon inherent to this model. This choice reflects the model's adeptness in synthesizing the virtues of k–ε and k–ω models within aerodynamic flows (Argyropoulos and Markatos, 2015). This synthesis lends precision to predicting adverse pressure gradients, a vital component of our investigation. The continuity equation (Eq. (1)) accounts for the fact that air entering a particular region must equal the mass of air exiting that region. In our context, it ensures that the inflow and outflow of air within the respiratory tract are in equilibrium, a crucial aspect in understanding the mechanics of respiration. Complementing the continuity equation, the momentum equation (Eq. (2)), derived from Newton's second law, offers a comprehensive view of how forces and pressure gradients shape the airflow. It delves into the complex interplay between mass flow, pressure, and acceleration within the respiratory tract.

The turbulent kinetic energy (Eq. (3)), often abbreviated as TKE, quantifies the energy associated with the chaotic and irregular motion of air particles within the turbulent flow. Understanding TKE distribution within the respiratory tract is vital for assessing the degree of turbulence, which, in turn, influences airflow patterns and pressure gradients. In parallel, the specific dissipation rate (Eq. (4)), often denoted as ε, characterizes the rate at which turbulent kinetic energy dissipates within the flow. This parameter provides insights into the dissipation of turbulent energy, essentially serving as a lens for the energy transformations that occur during the turbulent flow. The specific dissipation rate is fundamental in understanding how turbulence evolves and dissipates within the respiratory tract, offering a clear perspective on the dynamics of airflow and pressure gradients.

$$\frac{\partial \rho}{\partial t} + \nabla \bullet (\rho \boldsymbol{u}) = 0 \tag{1}$$

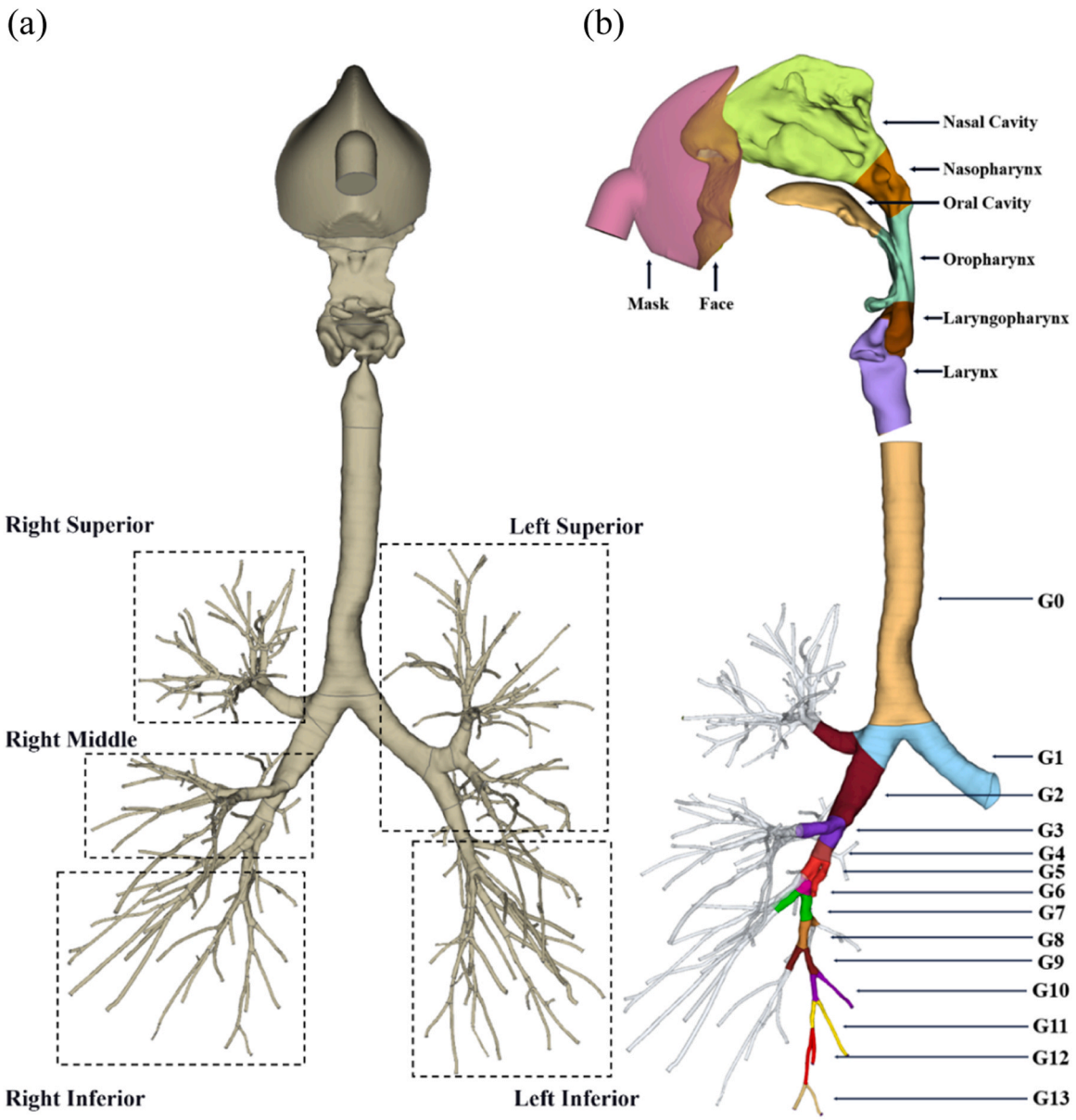

Fig. 1. Schematic representation of the computational model of the human respiratory tract. () Anterior viewpoint of the five lung lobes (b) Segmentation of anatomical regions within the model.

$$\frac{\partial \rho \boldsymbol{u}}{\partial t} + \nabla \bullet (\rho \boldsymbol{u}\boldsymbol{u}) = -\nabla p + \nabla \bullet (\bar{\tau}) + \rho \boldsymbol{g} \tag{2}$$

$$\frac{\partial (\rho k)}{\partial t} + \frac{\partial (\rho k u_i)}{\partial x_i} = \frac{\partial}{\partial x_j}\left[\left(\mu + \frac{\mu_t}{\sigma_k}\right)\frac{\partial k}{\partial x_j}\right] + P_k - Y_k + G_b \tag{3}$$

$$\frac{\partial (\rho \omega)}{\partial t} + \frac{\partial (\rho \omega u_i)}{\partial x_i} = \frac{\partial}{\partial x_j}\left[\left(\mu + \frac{\mu_t}{\sigma_\omega}\right)\frac{\partial \omega}{\partial x_j}\right] + P_\omega - Y_\omega + G_{\omega b} \tag{4}$$

2.3. Numerical framework

The respiratory tract's complex geometry poses a formidable computational modeling challenge. In response, the study adopted a polyhedral hybrid mesh with hexagonal prisms as boundary layers, amounting to approximately 0.23 million cells. The volume within our model, encompassing about 7.75 million cells, is assigned to irregular polyhedral cells. With an astute eye on regions marked by elevated turbulent intensity and those with delicate geometric intricacies, we have thoughtfully allocated a denser distribution of nodes. The average nodal distance within our mesh gradually declines from 0.4 mm in the upper airway to 0.35 mm in the trachea and primary bronchi and to 0.2 mm in the smaller branches of the bronchial tree. This configuration empowers our model to capture the near-wall fluid dynamics with precision. The result is a mesh design characterized by a changing boundary layer cell thickness (Fig. 2b).

Mesh independence involves systematically varying the mesh size or resolution to test whether the results of a simulation remain consistent as the mesh becomes finer. This rigorous process determines the point at which the simulation's outcome stabilizes, indicating that further mesh refinement would not significantly alter the results. In the context of our study, three distinct meshes were created, each advancing in refinement, and uniform simulation parameters were consistently applied. The analysis focuses on the oropharynx wall, extracting area-averaged static pressure values at three specific time intervals. The graphical representation of the findings illustrates that the parameter of interest undergoes minimal variations once the mesh cell count surpasses 6 million (Fig. 3). This observation affirms that the 7.97 million-cell mesh employed in this study unquestionably meets the criterion for mesh

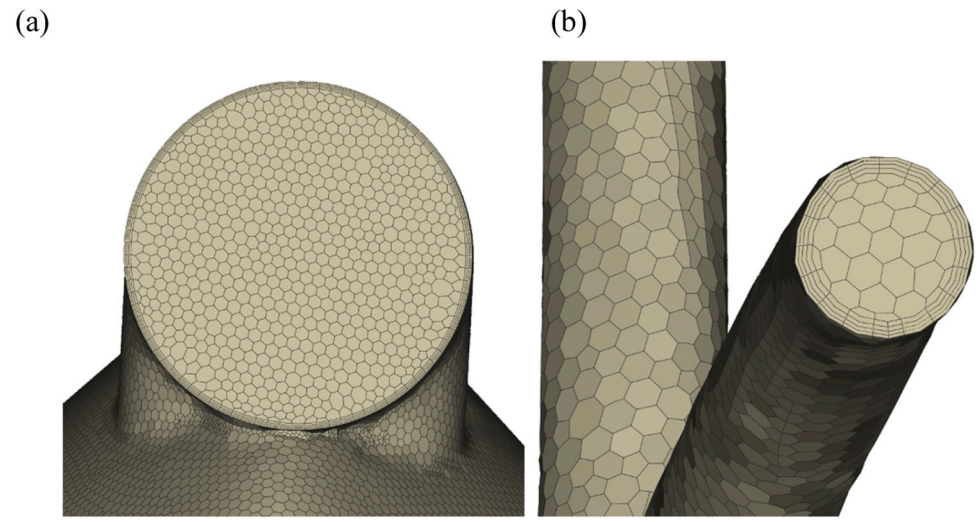

Fig. 2. Visual depiction of polyhedral mesh configuration with boundary layers. (a) Airflow inlet, housing the mask placement (b) Bronchial outlet, facilitating air discharge from the lung.

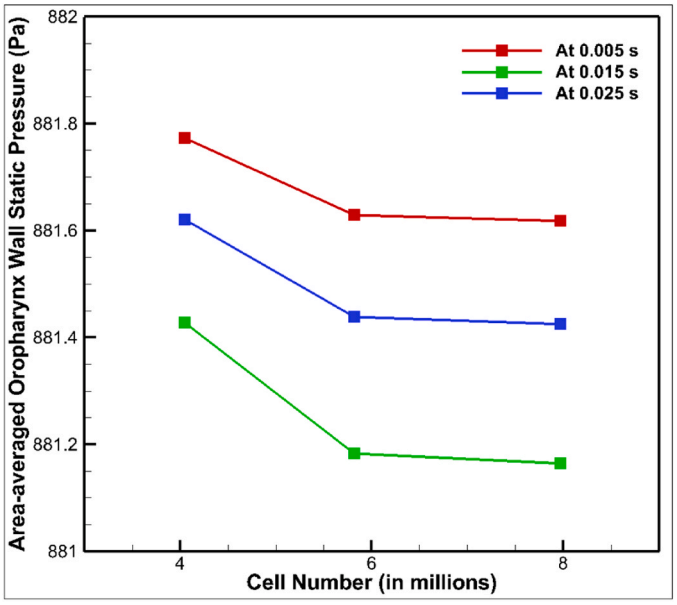

Fig. 3. Mesh independence showcasing the convergence behavior of area-averaged static pressure along the oropharynx wall across three distinct time intervals.

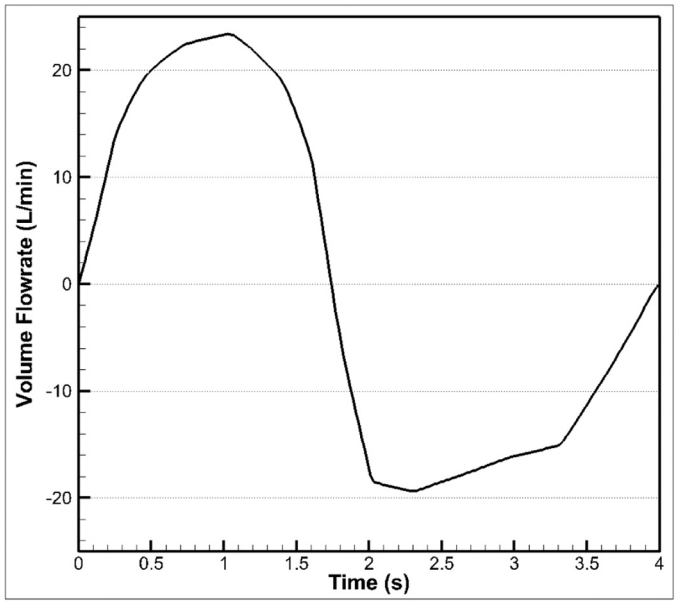

Fig. 4. Volume flow rate change during one breathing cycle at 7.5 L/min breathing rate, derived from multi-cycle-averaged experimental measurements of (Nishi, 2004). and implemented in CFD by Wedel et al. (2022).

independence.

The precise modeling of boundary conditions is the cornerstone of our methodology, dictating the dynamic behavior of airflow within the respiratory tract. At the mask inlet, a pressure of 882.6 Pa is established for cases involving CPAP, while at the nostril inlet, a pressure of 0 Pa is set for cases without CPAP. For the inlet conditions, velocity boundaries are determined using experimentally derived flow distributions specific to each lobe, showcasing 14.9, 24.5, 20.2, 8.3 and 32.1% for the left superior, left inferior, right superior, right middle, and right inferior lobes, respectively (Cohen et al., 1990). Our modeling approach ensures the uniformity of velocity magnitudes at the outlets of each lobe, thus upholding the consistent flow distribution throughout the simulation. As such, the velocity at the outlets of each lobe can be formulated as *Lobe Velocity = (Total volume flow rate × Flow percentage of the lobe) / Outlet area of the lobe*. To achieve this precision, we have devised two distinct functions, one for inhalation and another for exhalation. These functions, crafted through non-linear regression, closely approximates the volume flow rate profile (Fig. 4). They are then multiplied by the fraction of flow percentages and the respective outlet areas, yielding ten user-defined functions (UDFs). These UDFs are thoughtfully assigned to the outlets of each lobe, serving as precisely customized transient boundary conditions that reflect the intricacies of respiratory dynamics.

3. Results and discussion

In the context of OSAS, the pharynx undergoes a notable transformation, exhibiting a collapsible and highly compliant nature as the pharyngeal muscles relax. This physiological alteration reduces intraluminal pressure, leading to a consequential constriction of the cross-sectional area within the velopharyngeal airways. The velopharyngeal airways, the anatomical demarcation between the nasopharynx and oropharynx, hold significance in swallowing and speech (Cisonni et al.,

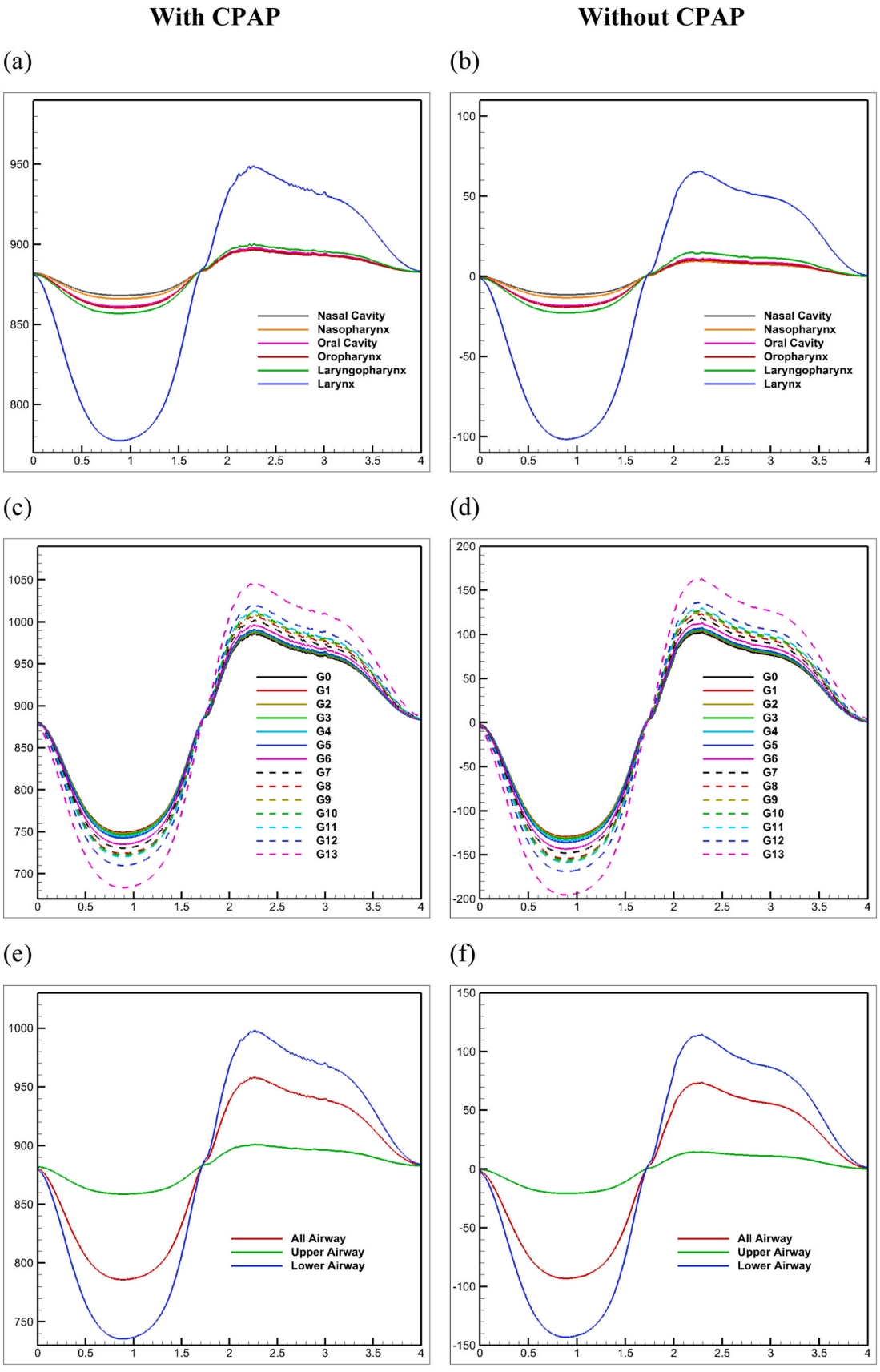

Fig. 5. Dynamic alterations in area-weighted static pressure (Pa) (y-axis) throughout a single respiratory cycle (x-axis representing time in seconds): (a) and (b) Upper airway regions; (c) and (d) Across lung generations; (e) and (f) Encompassing the entire respiratory geometry and upper versus lower airways.

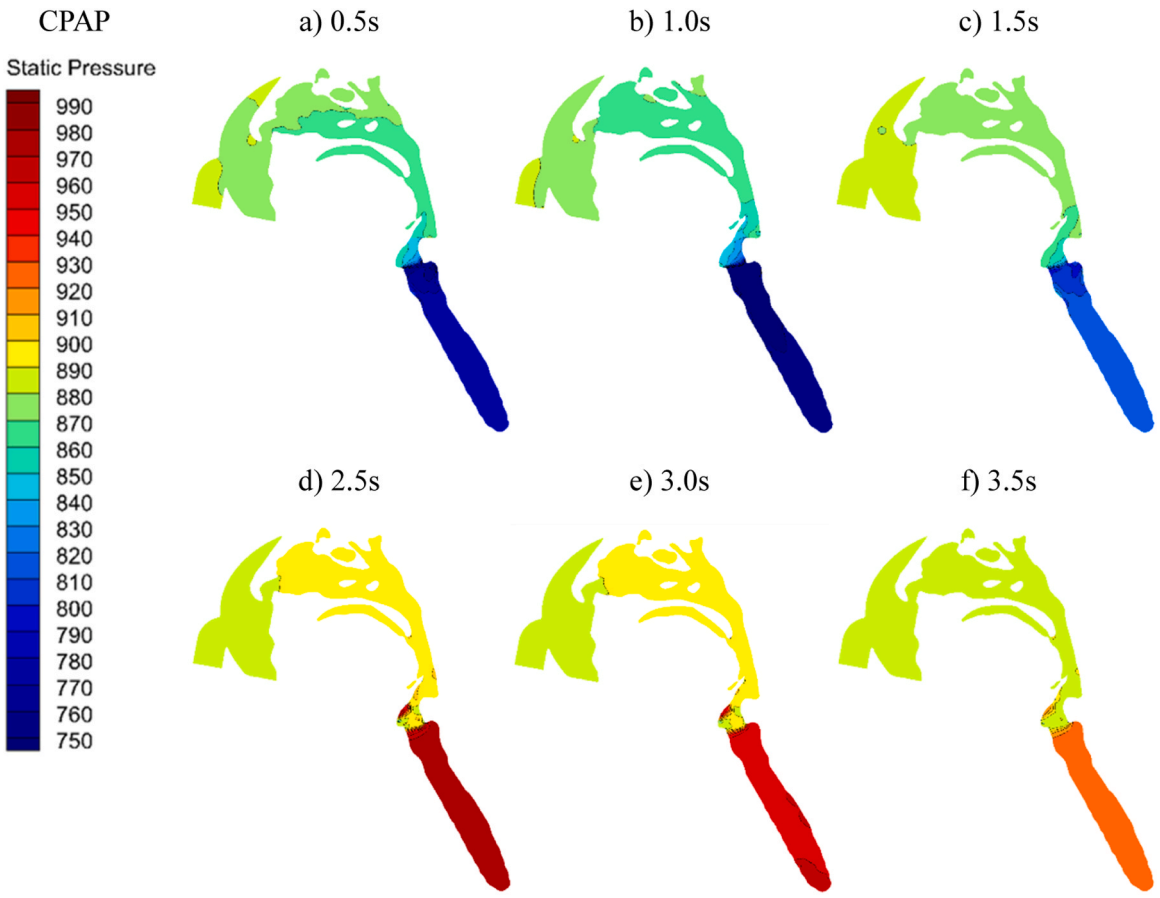

Fig. 6. Static pressure (Pa) contour on the central cross-sectional plane of the upper airway with CPAP: (a, b, and c) during the inhalation stage; (d, e, and f) during exhalation.

2013). Individuals afflicted by OSAS contend with an augmented pressure drop, particularly at the minimal cross-sectional point where the tonsils contribute to pharyngeal constriction (Taherian et al., 2019b). CPAP treatment addresses this physiological challenge, entailing the continuous supply of high-pressure airflow to sustain airway patency. Our study concentrates on the pharyngeal wall of OSAS patients under the influence of CPAP pressure, establishing a comparative analysis with healthy subjects devoid of OSAS and CPAP intervention.

3.1. *Pressure dynamics in upper and lower airways*

The static pressure in the upper airways is quantitatively and qualitatively presented in Figs. 5, 6 and 7 at distinct time instances for the upper and lower airways, obtaining a comparative analysis of lung airway pressure in the presence and absence of CPAP. This analysis mainly focuses on regions of critical interest: the oropharynx, laryngopharynx, and larynx. Notably, the profiles of area-weighted average wall static pressure (AWA WSP) exhibit remarkable uniformity across both scenarios. The larynx, in particular, displays the most substantial pressure fluctuations during both inhalation and exhalation, with readings peaking at 950 Pa and 65 Pa and dipping to lows of 780 Pa and −100 Pa, with and without the application of CPAP, respectively. The remaining regions, encompassing the nasal cavity, nasopharynx, oral cavity, oropharynx, and laryngopharynx, exhibit consistent patterns during the breathing cycle, maintaining pressure values that fall within the range of 850–900 Pa with CPAP and −20–20 Pa without CPAP. Additionally, the pressure differentials experienced between the nasal cavity and the larynx in both scenarios mirror each other, showing a maximum drop of approximately 100 Pa during inhalation and 50 Pa during exhalation.

The larynx's pressure profile mirrors the subsequent lung generations, from the trachea (G0) to the 14th lung generation (G13), as depicted in Figs. 4c and 4d. Among these, the 14th lung generation exhibits the most pronounced pressure variations, oscillating between 660 Pa and 870 Pa during inhalation and 800–1040 Pa during exhalation in the CPAP scenario. Without CPAP, the total pressure range spans from −200–160 Pa over the breathing cycle. Negative pressure values during inhalation denote the inward air flow into the respiratory tract, with the most distal lung generations registering the lowest pressures. Conversely, as air is expelled from the lungs, the flow reverses during exhalation, initiating from the distal generations. Here, the highest pressure is observed at G13, while G0 records the lowest. The concave upward and downward patterns characterizing the pressure profiles of the lung regions and generations during inhalation and exhalation underscore the inversely proportional yet intricately connected velocity-pressure relationship.

Given the paramount importance of upper airway pressure in CPAP application, Figs. 5e and 5f consolidate the regions of interest into a single cluster called the "Upper airway." The curve closely follows the slightly varying trend observed in its constituent regions. The pressure of the upper airways can be seen varying in Figs. 6 and 7 at three distinct time instances during inhalation as the pressure moves from higher region to lower and three instances during exhalation where the pressure increases from lower areas to higher. The inhalation process commences with diaphragm contraction and thoracic cavity expansion, generating a lower intrapulmonary pressure than atmospheric pressure. This establishes a pressure gradient from the upper airway to the lower airway. Pressure gradually diminishes as airflow descends through the respiratory tract, including the trachea, bronchi, and bronchioles. This pressure reduction correlates with the concurrent increase in cross-sectional area

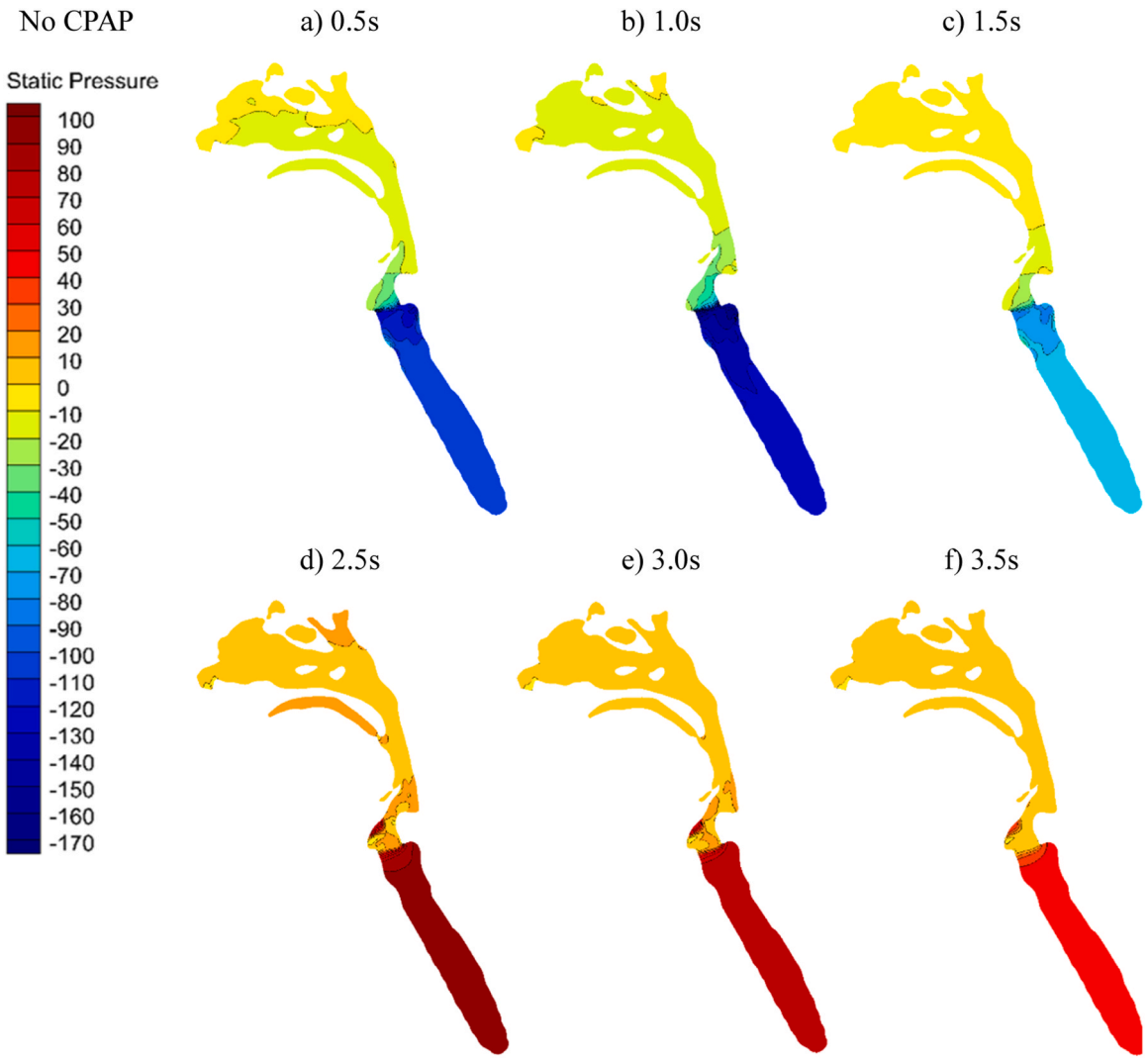

Fig. 7. Static pressure (Pa) contour on the central cross-sectional plane of the upper airway without CPAP: (a, b, and c) during the inhalation stage; (d, e, and f) during exhalation.

within the lower airways. This alignment provides a consistent and anatomically grounded explanation for the observed phenomenon.

To provide further clarity and enable a comparative assessment spanning the entire lung, the lung generations are grouped into a collective entity termed the "Lower airway," with the combination of all airways collectively referred to as the "All airway." It is observed that the pressure dynamics within the lower airway predominantly adhere to the fluctuating pressure curve of the lung generations, with the entire airway pressure profile markedly influenced by the lower airway dynamics.

3.2. Velocity of upper airway

With and without CPAP treatment, the patient inhales and exhales on average around 7.5 L/min, with the variation during the middle of each inhalation and exhalation phase reaching above 20 L/min. As the regular breathing volume flow rate representing the velocity magnitude follows a steep increase towards the middle of the inhalation followed by a steep decrease at the end, the velocity in the Z direction (vertically upward) exhibits higher values reaching 3 m/s in the nasal cavity at 0.5 s (Fig. 8a-c). At the regions of interest where the cross-sectional area naturally narrows, the Z velocity arises to [4–7 m/s] with a negative sign indicating the presence of circulating flow. At the trachea, where the cross-section widens again, the velocity regresses to similar values in the nasal cavity. As the exhalation phase commences with a steep increase in velocity at 2.5 s, the pattern follows similar to the inhalation phase where near 3 m/s values are observed in the trachea and nasal cavity with a decreasing trend from 2.5 s to 3.5 s, and the oropharynx, velopharynx, and larynx experiencing the highest values of [6–11 m/s] (Fig. 8d-f). The velocity pattern and magnitude are unaffected by the application of CPAP due to the impertinence of the positive pressure on the airflow volume flow rate, as the pressure drop remains equal for both cases during inhalation and exhalation (Figs. 5e, 5f)

3.3. Airway shear stress

When administering CPAP to patients with OSAS, safeguarding lung tissue integrity is paramount to mitigate potential complications. High shear stress (> 1.5 Pa) exerted on the lung's surface can have deleterious effects on lung cells, possibly leading to apoptosis (Chen et al., 2015).

In this context, the area-weighted average lung shear stress with and without CPAP is calculated to ascertain the safety of its application. Due to the direct dependence of shear stress on velocity gradients, which remain unchanged with CPAP, the shear stress levels in the upper, lower, and entire airway remain unaffected by CPAP, affirming its benign impact on the lung surface (Fig. 9a, b). The lower airway, spanning lung generations G0 to G13, experiences higher shear stress values than the upper airway. Both upper and lower airways follow a pattern consistent

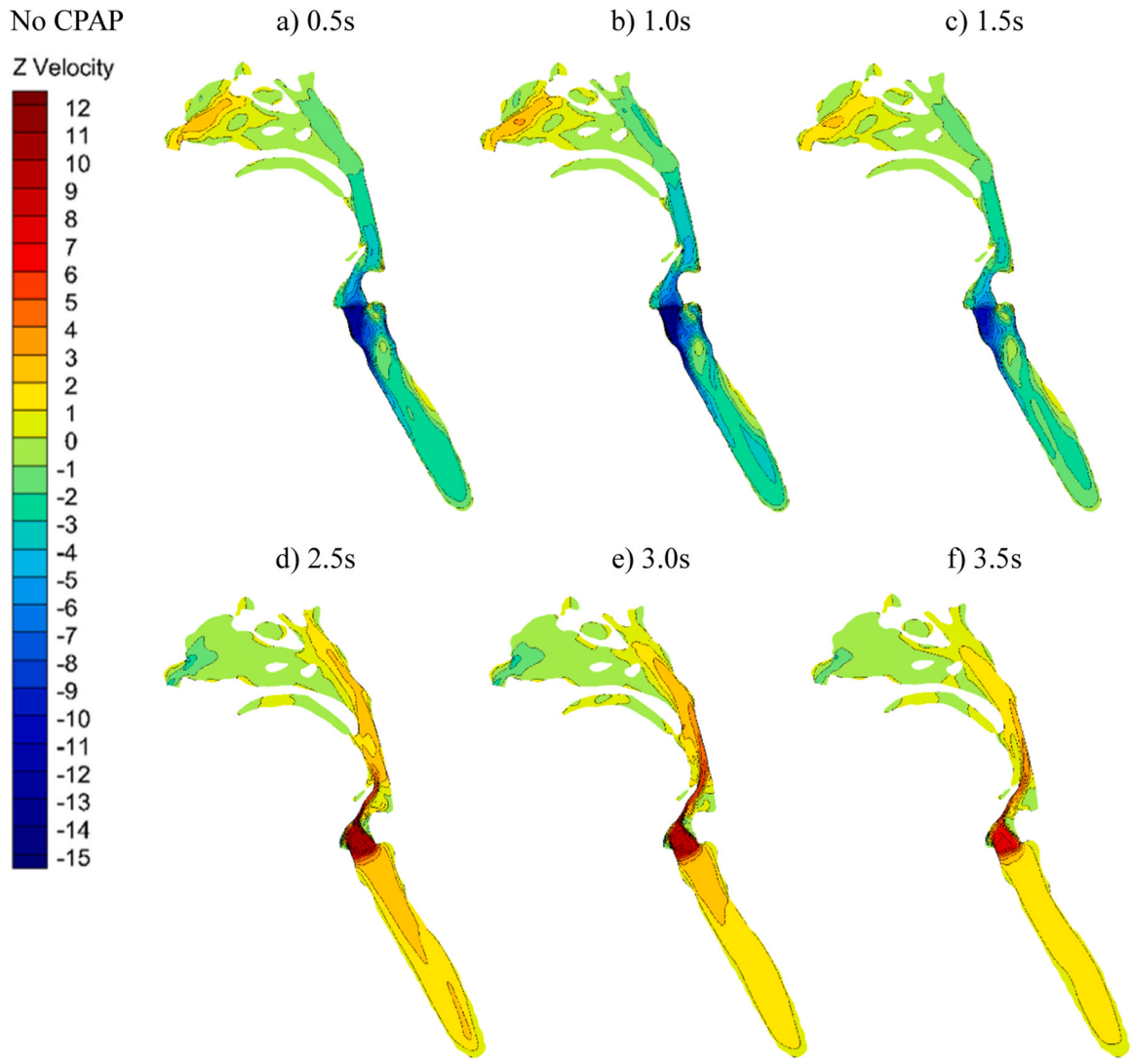

Fig. 8. Vertically upward Z velocity (m/s) contour on the central cross-sectional plane of the upper airway without CPAP: a) b) and c) during the inhalation stage; d) e) and f) during exhalation.

with the volume flow rate. In the lower airway, shear stress reaches a maximum of 0.17 Pa during inhalation and 0.125 Pa during exhalation. In comparison, the upper airway registers a maximum of 0.125 Pa during inhalation and 0.11 Pa during exhalation. The combined effect on the entire airway, referred to as 'All airway,' demonstrates a nearly equal influence from both regions.

Examining specific regions within the upper airway, the larynx exhibits the highest shear stress, with a maximum of 0.7 Pa during inhalation, followed by the laryngopharynx and oropharynx (Fig. 9c). The oral cavity records negligible values, as airflow bypasses it, originating from the nasal cavity. The gradual increase in shear stress from the nasal cavity to the larynx is attributed to the progressively constricting cross-sectional area, leading to higher velocity gradients and, consequently, elevated shear stress. This pattern continues through the lung generations, with G13 displaying the highest shear stress (a maximum of 0.34 Pa) and G1 the lowest (a maximum of 0.08 Pa) (Fig. 9d).

It is essential to underscore the relationship between shear stress magnitude and airflow velocity, which depends on dynamic fluid viscosity and velocity gradients near the surface. The Venturi effect, encountered when fluid passes through a narrowed conduit, corresponds to the airflow through the vocal cords in the larynx within the respiratory system. The constriction of this passage results in a marked escalation of both velocity and near-wall velocity gradients, leading to a significant increase in shear stress. This phenomenon clarifies the prominent peak in shear stress observed within the larynx. Conversely, the shear stress in the oral cavity remains substantially low. This is attributable to the mouth's closure, effectively creating a "cave" with an opening perpendicular to the airflow velocity vector. Consequently, the airflow entering the oral cavity is minimal in this configuration. This reduced airflow velocity, coupled with a decrease in the near-wall velocity gradient, yields the observed low shear stress values.

3.4. Surface normal forces

The area-weighted averaged wall normal force (AWA WNF) quantifies the impact of surface static pressure on the internal surfaces of different regions within the airway. This force represents a direct and fundamental indicator of the support provided by CPAP's supporting function on the collapsing airway in preventing airway collapse. A comprehensive analysis in Fig. 10 reveals that applying CPAP results in a notable increase in surface normal force. During both inhalation and exhalation, the airways with CPAP exhibit positive wall normal forces, with the nasal cavity experiencing the highest force (13.82 N and 14.10 N during inhalation and exhalation, respectively), while the nasopharynx registers the lowest force (1.71 N and 1.93 N during inhalation and exhalation, respectively). In contrast, the airways

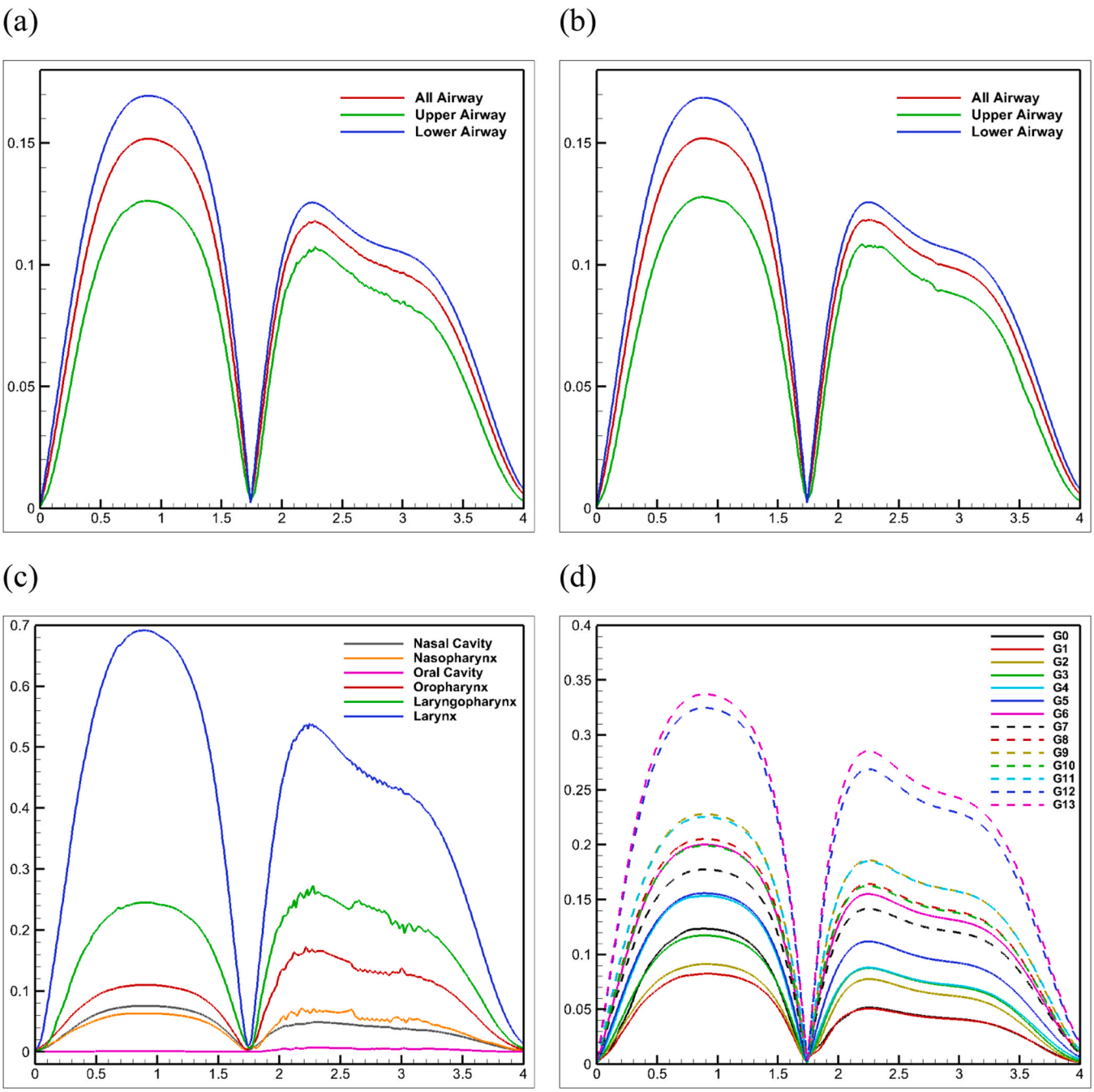

Fig. 9. Dynamic changes in area-weighted average wall shear stress (Pa) (y-axis) throughout a single respiratory cycle (x-axis representing time in seconds): (a) & (b) upper, lower sections, and entire airway with and without CPAP, respectively; (c) regions of the upper airway with CPAP; (d) lung generations with CPAP.

without CPAP exhibit fluctuating normal forces. Specifically, during inhalation, the airways without CPAP experience negative wall normal forces, with the nasopharynx bearing the highest negative force (-0.014 N) and the larynx the lowest (-0.140 N). Conversely, during exhalation, the airways with CPAP receive positive wall normal forces, with the nasal cavity displaying the highest positive force (0.091 N) and the nasopharynx the lowest (0.009 N). It is pertinent to note that the nasopharynx often plays a critical role in the context of airway collapse during OSAS. The above comparative analysis emphasizes that CPAP intervention can provide an average increase of two orders of magnitude in wall normal force acting on the internal surface of the nasopharynx. This enhancement effectively augments the supportive forces crucial for preventing airway collapse. More significantly, it is revealed that airways with CPAP receive positive normal forces during inhalation, while those without CPAP experience negative normal forces, exacerbating the propensity for airway collapse as the negative force effectively acts as a suction force.

4. Conclusion

During one respiration cycle, the aerodynamic characteristics of a complete human respiratory tract under normal atmospheric pressure and continuous positive airway pressure of 9 cm H_2O (882.6 Pa) were investigated. The main findings of this study are summarized as follows:

- An intriguing revelation emerged when comparing the static pressure profiles of healthy subjects to those undergoing CPAP treatments. CPAP cases exhibited substantially higher static pressure

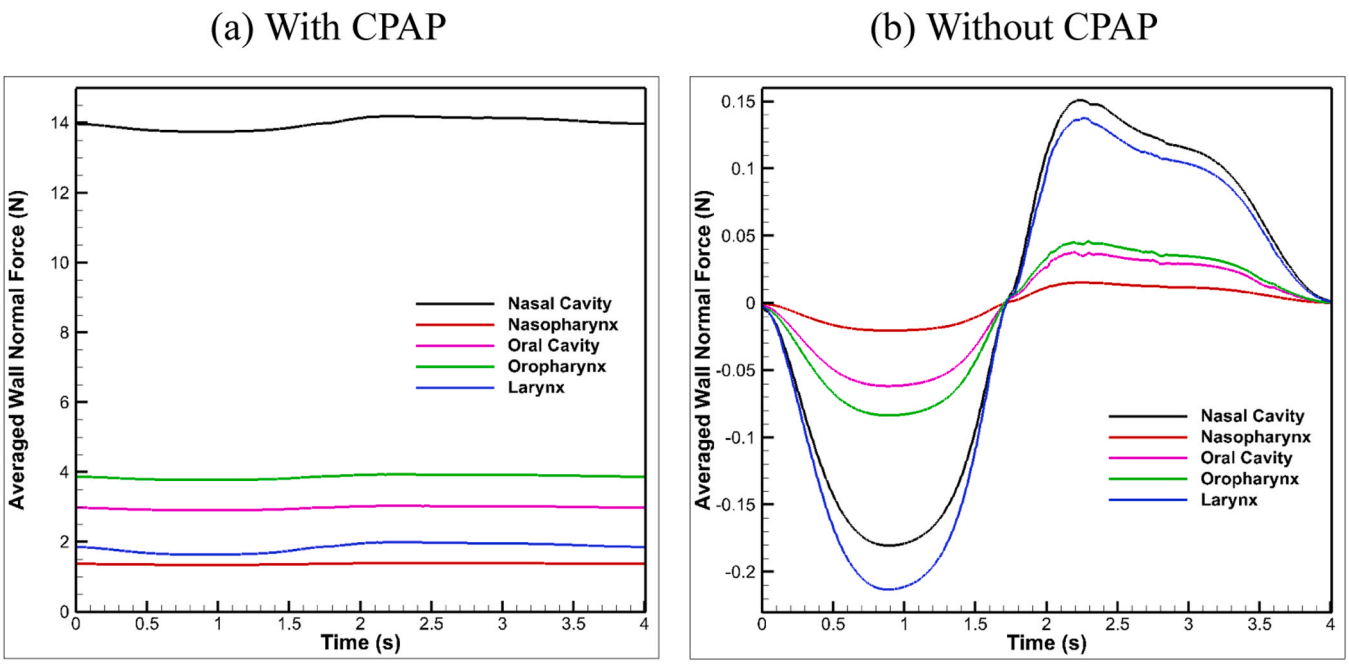

Fig. 10. Dynamic variations in surface normal forces (N) (y-axis) throughout a single respiratory cycle (x-axis representing time in seconds) in the upper airway regions: (a) with CPAP-assisted breathing and (b) Absence of CPAP.

levels both during inhalation and exhalation. This stark contrast highlights the critical role of CPAP in mitigating OSAS, emphasizing that it provides the critical pressure support required to alleviate airway constriction.

- While CPAP primarily focuses on increasing the airway pressure, its influence on velocity patterns within the upper airway was observed to be relatively marginal. There is no noticeable difference between the velocity field of a respiratory tract with and without CPAP apart from the small variation introduced by the face mask.
- One of the paramount concerns in CPAP therapy is the potential impact on shear stress levels within the respiratory tract, as elevated shear stress can be detrimental to lung tissues. The research findings, however, offer assurance. CPAP's application appeared to have a minimal effect on shear stress levels, suggesting that it is a safe therapeutic approach that mitigates potential lung cell damage.
- Observation indicates that the larynx emerges as the region experiencing the highest shear stress within the upper airway. This phenomenon can be attributed to the naturally narrowed cross-sectional area of the upper airway in this region.
- The application of CPAP significantly enhances the supporting forces on the airway wall, with airways under CPAP conditions experiencing positive forces during both inhalation and exhalation. In contrast, airways without CPAP exhibit fluctuating normal forces, including negative forces during inhalation, which exacerbate airway collapse by acting as suction forces.

This comprehensive investigation highlights the crucial significance of CPAP in treating OSAS, largely by promoting the maintenance of an open airway without excessive strain on airway tissues. The findings significantly contribute to our understanding of the complex physiological changes brought about by CPAP treatment, reinforcing its effectiveness and significance in the context of OSAS therapy.

Ethics approval

The creation of this model has been approved ethically by the Human Research Ethics Committees at the University of Technology Sydney. Specifically, our research, which involved the utilization of human CT scans, has received ethical approval, denoted by reference ETH23–8670, granted on 7 September 2023.

Funding

The work of author Xinlei Huang (黄新磊) is supported by the China Scholarship Council (ID: 202208410137).

CRediT authorship contribution statement

Goutam Saha: Writing – review & editing, Investigation, Formal analysis. **Suvash C Saha:** Writing – review & editing, Supervision, Project administration, Formal analysis, Conceptualization. **Xinlei Huang:** Writing – original draft, Software, Methodology, Investigation. **Isabella Francis:** Writing – review & editing, Visualization, Formal analysis.

Data Availability

No data was used for the research described in the article.

Acknowledgments

The authors would like to acknowledge the computing facility at the University of Technology Sydney (UTS). The authors used AI-assisted technology (ChatGPT 4) for language editing and grammar checking.

Appendix A. Geometric parameters of the respiratory tract model

Table 4
Surface area, volume, number of inlets, outlets, and regions in our respiratory tract geometry.

Inlet	Surface Area (mm^2)	Number
Mask tube inlet	212.82	1
Outlets	**Surface Area (mm^2)**	**Number**
Right superior lobe outlets	54.59	49
Right middle lobe outlets	26.53	23
Right inferior lobe outlets	53.08	47
Left superior lobe outlets	57.94	57
Left inferior lobe outlets	62.01	52
Total outlets	254.15	228
Region	**Surface Area (mm^2)**	**Volume (mm^3)**
Mask and Face	11,551.10	50,300.12
Nasal Cavity	15,830.99	26,452.22
Nasopharynx	1547.97	5537.52
Oropharynx*	4381.87	10,101.08
Oral Cavity	3373.54	5455.17
Larynx	2098.43	5614.45
Trachea	5547.77	21,742.69
Primary Bronchi	1991.67	6094.52
Secondary Bronchi	1701.79	4071.09
Tertiary Bronchi	1982.72	4962.23
right superior lobe	4225.43	1765.20
right middle lobe	3163.99	1615.57
right inferior lobe	7047.43	3946.46
left superior lobe	6803.61	3066.26
left inferior lobe	6837.88	3474.33
Total	66,535.09	103,898.79

*With partial laryngopharynx

References

Abdullayev, A., Tekeli, O., Yanık, Ö., Acıcan, T., Gülbay, B., 2019. Investigation of the presence of glaucoma in patients with obstructive sleep apnea syndrome using and not using continuous positive airway pressure treatment. Turk. J. Ophthalmol. 49 (3), 134–141.

Argyropoulos, C.D., Markatos, N.C., 2015. Recent advances on the numerical modelling of turbulent flows. Appl. Math. Model. 39 (2), 693–732.

Chen, Z.-l, Song, Y.-l, Hu, Z.-y, Zhang, S., Chen, Y.-z, 2015. An estimation of mechanical stress on alveolar walls during repetitive alveolar reopening and closure. J. Appl. Physiol. 119 (3), 190–201.

Cisonni, J., Lucey, A.D., King, A.J., Islam, S.M., Lewis, R., Goonewardene, M.S., 2015. Numerical simulation of pharyngeal airflow applied to obstructive sleep apnea: effect of the nasal cavity in anatomically accurate airway models. Med Biol. Eng. Comput. 53 (11), 1129–1139.

Cisonni, J., Lucey, A.D., Walsh, J.H., King, A.J., Elliott, N.S., Sampson, D.D., Eastwood, P. R., Hillman, D.R., 2013. Effect of the velopharynx on intraluminal pressures in reconstructed pharynges derived from individuals with and without sleep apnea. J. Biomech. 46 (14), 2504–2512.

Cohen, B.S., Sussman, R.G., Lippmann, M., 1990. Ultrafine particle deposition in a human tracheobronchial cast. Aerosol Sci. Technol. 12 (4), 1082–1091.

Gambino, F., Zammuto, M.M., Virzì, A., Conti, G., Bonsignore, M.R., 2022. Treatment options in obstructive sleep apnea. Intern. Emerg. Med. 17 (4), 971–978.

Huang, X., Clemon, L.M., Islam, M.S., C. Saha, S., 2022. Optimization of fluid characteristics in the main nozzle of an air-jet loom. Text. Res. J. 92 (3-4), 525–538.

Huang, R., Li, X., Rong, Q., 2013. Control mechanism for the upper airway collapse in patients with obstructive sleep apnea syndrome: a finite element study. Sci. China Life Sci. 56 (4), 366–372.

Huang, X., Saha, S.C., Saha, G., Francis, I., Luo, Z., 2024. Transport and deposition of microplastics and nanoplastics in the human respiratory tract. Environ. Adv. 16, 100525.

Jeong, S.J., Kim, W.S., Sung, S.J., 2007. Numerical investigation on the flow characteristics and aerodynamic force of the upper airway of patient with obstructive sleep apnea using computational fluid dynamics. Med Eng. Phys. 29 (6), 637–651.

Lu, M.Z., Liu, Y., Ye, J.Y., Luo, H.Y., 2014. Large eddy simulation of flow in realistic human upper airways with obstructive sleep. Procedia Comput. Sci. 29, 557–564.

Luo, H., Sin, S., McDonough, J.M., Isasi, C.R., Arens, R., Wootton, D.M., 2014. Computational fluid dynamics endpoints for assessment of adenotonsillectomy outcome in obese children with obstructive sleep apnea syndrome. J. Biomech. 47 (10), 2498–2503.

M. Nishi, Breathing of Humans and its Simulation, LSTM-Erlangen Institute of Fluid Mechanic Friedlich-Alexander-University Erlangen, (2004).

Rahim, W.M., Nik Ghazali, N.N., Khor, C.Y., Zainon, M., Kamangar, S., Ibrahim, N., Razi, R., 2021. Computational analysis of airflow in upper airway under light and heavy breathing conditions for a realistic patient having obstructive sleep Apnea. Comput. Model. Eng. Sci. 127, 1–22.

Reynor, A., McArdle, N., Shenoy, B., Dhaliwal, S.S., Rea, S.C., Walsh, J., Eastwood, P.R., Maddison, K., Hillman, D.R., Ling, I., Keenan, B.T., Maislin, G., Magalang, U., Pack, A.I., Mazzotti, D.R., Lee, C.H., Singh, B., 2022. Continuous positive airway pressure and adverse cardiovascular events in obstructive sleep apnea: are participants of randomized trials representative of sleep clinic patients? Sleep 45 (4).

Saha, S., Francis, I., Huang, X., Paul, A., 2022. Heat transfer and fluid flow analysis of realistic 16-generation lung. Phys. Fluids 34.

Saha, S.C., Francis, I., Saha, G., Huang, X., Molla, M.M., 2024. Hemodynamic insights into abdominal aortic aneurysms: bridging the knowledge gap for improved patient care. Fluids 9 (2), 50.

Strohl, K.P., Butler, J.P., Malhotra, A., 2012. Mechanical properties of the upper airway. Compr. Physiol. 2 (3), 1853–1872.

Suga, H., Iwasaki, T., Mishima, K., Nakano, H., Ueyama, Y., Yamasaki, Y., 2021. Evaluation of the effect of oral appliance treatment on upper-airway ventilation conditions in obstructive sleep apnea using computational fluid dynamics. Cranio 39 (3), 209–217.

Taherian, S., Rahai, H., Lopez, S., Shin, J., Jafari, B., 2019b. Evaluation of human obstructive sleep apnea using computational fluid dynamics. Commun. Biol. 2 (1), 423.

Taherian, S., Rahai, H., Lopez, S., Shin, J., Jafari, B., 2019a. Evaluation of human obstructive sleep apnea using computational fluid dynamics. Commun. Biol. 2, 423.

Wakayama, T., Suzuki, M., Tanuma, T., 2016. Effect of nasal obstruction on continuous positive airway pressure treatment: computational fluid dynamics analyses. PLoS One 11 (3), e0150951.

Wedel, J., Steinmann, P., Štrakl, M., Hriberšek, M., Cui, Y., Ravnik, J., 2022. Anatomy matters: the role of the subject-specific respiratory tract on aerosol deposition - A CFD study. Comput. Methods Appl. Mech. Eng. 401, 115372.

Wootton, D.M., Luo, H., Persak, S.C., Sin, S., McDonough, J.M., Isasi, C.R., Arens, R., 2014. Computational fluid dynamics endpoints to characterize obstructive sleep apnea syndrome in children. J. Appl. Physiol. (1985) 116 (1), 104–112.

Xu, C., Sin, S., McDonough, J.M., Udupa, J.K., Guez, A., Arens, R., Wootton, D.M., 2006. Computational fluid dynamics modeling of the upper airway of children with obstructive sleep apnea syndrome in steady flow. J. Biomech. 39 (11), 2043–2054.

Yu, C.C., Hsiao, H.D., Tseng, T.I., Lee, L.C., Yao, C.M., Chen, N.H., Wang, C.J., Chen, Y. R., 2012. Computational fluid dynamics study of the inspiratory upper airway and clinical severity of obstructive sleep apnea. J. Craniofac Surg. 23 (2), 401–405.

Zhao, M., Barber, T., Cistulli, P., Sutherland, K., Rosengarten, G., 2013. Computational fluid dynamics for the assessment of upper airway response to oral appliance treatment in obstructive sleep apnea. J. Biomech. 46 (1), 142–150.

Zhu, L., Liu, H., Fu, Z., Yin, J., 2019b. Computational fluid dynamics analysis of H-uvulopalatopharyngoplasty in obstructive sleep apnea syndrome. Am. J. Otolaryngol. 40 (2), 197–204.

Zhu, L., Liu, H., Fu, Z., Yin, J., 2019a. Computational fluid dynamics analysis of H-uvulopalatopharyngoplasty in obstructive sleep apnea syndrome. Am. J. Otolaryngol. 40 (2), 197–204.